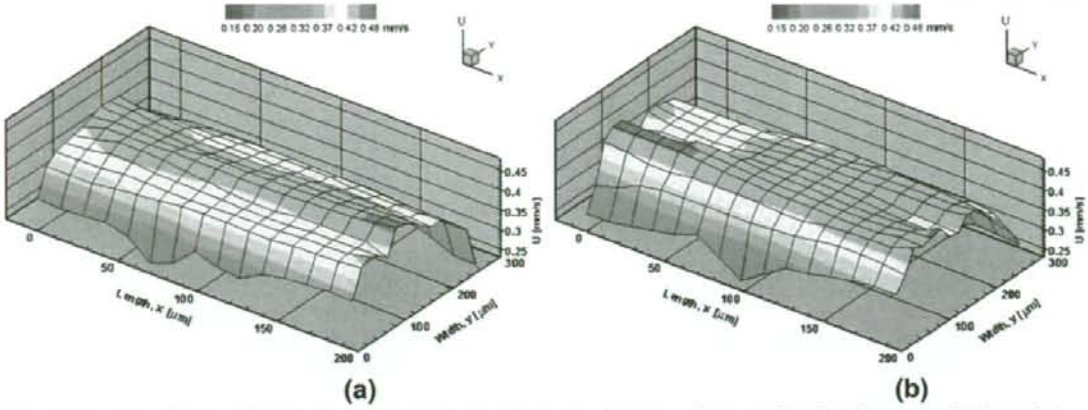

Fig. 12 Ensemble velocity profiles (U) of two representative samples in the middle plane for *in vitro* blood. (**a**) Sample 1 and (**b**) sample 2

the rectangular microchannel with y and z cross section is the following (Bruus 2004; Mortensen et al. 2005):

$$u_x(y,z) = \frac{48Q}{\pi^3 hw} \frac{\sum_{n,\text{odd}}^{\infty} \frac{1}{n^3}\left[1 - \frac{\cosh\left(n\pi\frac{y}{h}\right)}{\cosh\left(n\pi\frac{w}{2h}\right)}\right] \sin\left(n\pi\frac{z}{h}\right)}{\left[1 - \sum_{n,\text{odd}}^{\infty} \frac{192/\pi}{n^5\pi^5 w} \tanh\left(n\pi\frac{w}{2h}\right)\right]}, \quad (5)$$

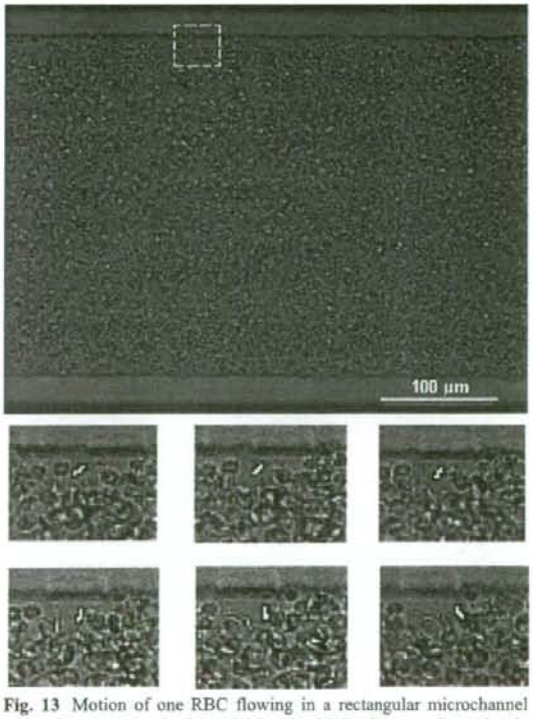

Fig. 13 Motion of one RBC flowing in a rectangular microchannel with a low aspect ratio (h/w=0.15). The RBC of interest has a *bright grey colour* in its central region. All images were captured with a 20× objective lens

where u_x is the fluid velocity in the x-direction, y and z are the directions normal to the flow, w and h are the width and depth of the microchannel, respectively, and Q is the flow rate.

Figures 5 and 6 compare the theoretical estimates using Eq. 5 and the average fluid velocities of 100 PIV image pairs for several optically sectioned planes along the microchannel depth. The PIV measurements were obtained with an exposure time of 4,995 μs, magnification factor (pixels/μm) of 0.86, and time interval of 5ms between two images.

Generally, the experimental results shown in Figs. 5 and 6 were in good agreement with the analytical solution, especially the results at the middle plane (z = 22.5 μm), where we found errors less than 5% (Fig. 5). As one moves out of the middle plane, the deviations start to increase and at locations close to the wall, the errors were about 7% (Fig. 6).

3.2 Blood flow

3.2.1 Ensemble-averaged velocity profiles

In addition to examining PS, we studied the behavior of *in vitro* blood (RBCs in PS, 20% Hct) through the rectangular PDMS microchannel. An example of a recorded image (halogen illumination source) of the *in vitro* blood flow is presented in Fig. 7(a). Figure 7(b) displays an image with both RBCs (halogen illumination) and fluorescent particles (laser-emitted light). The latter image could be used to calculate the velocity fields of the *in vitro* blood flow.

Figures 8 and 9 compare the mean velocity profiles of 100 ensemble image pairs for PS and *in vitro* blood (20% Hct), from six different measurements recorded at different x–y planes, spaced at 5-μm-depth intervals (z-direction). Both results were obtained under the same experimental conditions (Re = 0.02).

From Figs. 8 and 9, the velocity profiles of the PS fluid in several horizontal planes (x–y axis) clearly show that the

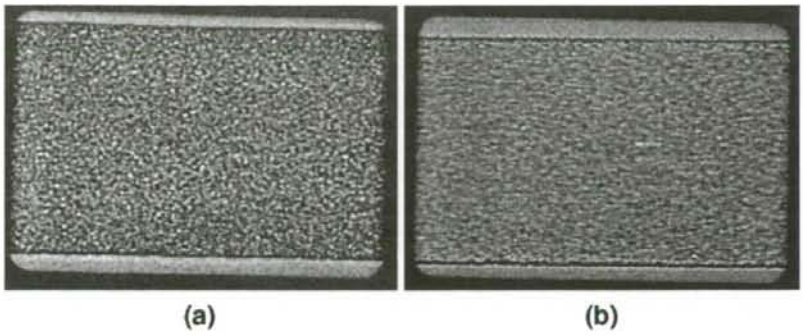

Fig. 14 Flow of RBCs (~20% Hct) suspended in PS through a rectangular PDMS microchannel 300 μm wide and 45 μm deep for a (**a**) Re ~0.02; (**b**) Re ~0.1

flow is stable and fully developed. In addition, Figs. 8 and 9 also show that for PS fluid, the shape of the mean velocity profile is markedly blunt in the middle region. However, examining the average velocity profiles of the *in vitro* blood, small deviations between the fluids were observed, especially in the regions near the walls. These small perturbations along the width of the microchannel become much clearer on analyzing the 3-D profiles shown in Fig. 10. Figure 10(a) indicates that the PS velocity profile along the z-direction had a smooth parabolic shape, whereas the *in vitro* blood flow (Fig. 10(b)) was characterized by a velocity profile containing several small disturbances along the z-direction.

3.2.2 Ensemble velocity profiles in the middle plane

It is generally agreed that the ensemble average velocity process improves the reliability and accuracy of PIV measurements because of the improvement in the signal-to-noise ratio and the reduction of measurement errors associated with the Brownian motion of the tracer particles and some possible "bottleneck" effects of the syringe pump. Furthermore, our experimental confocal PIV results with the PS fluid compared to the theoretical model (Fig. 5) showed the best agreement was in the middle plane of the microchannel (z = 22.5 μm) because of a reduction in several effects resulting from the microchannel wall (interaction between particle and wall, roughness of the wall, etc.). The PIV measurements in the middle plane seemed to generate results closer to the true velocity profile present in the rectangular PDMS microchannel. In this study, 6 samples of 100 PIV image pairs at the middle plane were analyzed for both PS and *in vitro* blood (~20% Hct). Figures 11 and 12 show the time-averaged velocity profiles (U) along a certain length (150 μm) from two different representative samples for PS and *in vitro* blood, respectively.

Figure 11 shows that when using PS fluid, a markedly smooth, flat profile tended to develop along the rectangular microchannel. However, for the *in vitro* blood flow, small perturbations in the shape of the ensemble velocity profiles were observed (Fig. 12). These qualitative observations can play an important role in providing reliable information on the time-averaged flow behavior over a specific period of interest.

3.2.3 RBC flow visualization

To determine possible causes of the perturbations in the velocity profiles of the *in vitro* blood flowing in the rectangular microchannel, RBC motion was visualized with halogen illumination from our confocal micro-PIV system. Figure 13 shows the dynamic behavior of the RBCs in a rectangular microchannel with a low aspect ratio. Figure 13

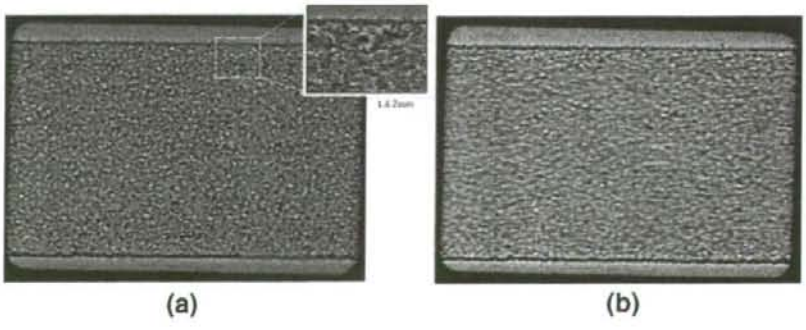

Fig. 15 Flow of RBCs (~20% Hct) suspended in dextran 40 (Dx-40) through a rectangular PDMS microchannel 300 μm wide and 45 μm deep for a (**a**) Re ~0.01; (**b**) Re ~0.08

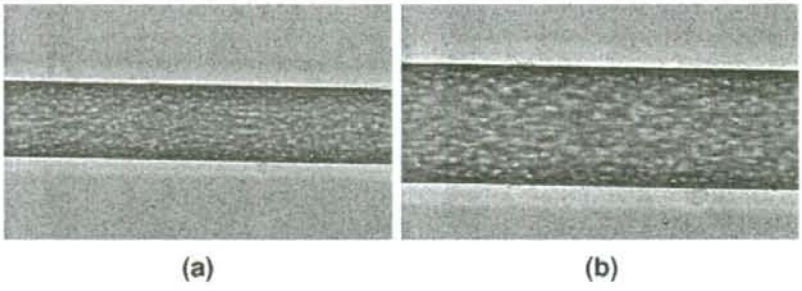

Fig. 16 Flow of RBCs (~20% Hct) suspended in dextran 40 (Dx-40) through a rectangular PDMS microchannel 100 μm wide and 62 μm deep for a Re of ~0.03 (**a**) 20× objective lens; (**b**) 32× objective lens

also shows detailed consecutive halogen images captured at time intervals of 10ms, when the motion of one particular RBC was followed.

During the capture of the images, we did not observe any significant plasma layer, but rather a homogeneous distribution of the RBCs. Furthermore, in the central region of the microchannel (shear rate close to zero), the RBCs tended to move along with the flow with a regular rotational motion, retaining their biconcave shape. Near to the wall, where the shear rate increases significantly, both rotational and tumbling motions accompanied by membrane deformation were observed (see detailed consecutive images in Fig. 13). Interactions between neighboring RBCs at different depth planes (boundary layers) were also observed along the full microchannel.

3.2.4 Plasma layer

The formation of a plasma-rich layer located between the RBC core and wall is well documented in glass microchannels with diameters less than 300 μm (Faharaeus and Lindqvist 1931; Chien et al. 1984; Maeda 1996; Pries and Secomb 2003). However, to our knowledge the effect of both geometry and suspension medium in a straight rectangular PDMS microchannel has not been investigated. In an effort to understand why we observed no plasma layer in our microchannel, first we investigated the effect of the flow rate on the formation of the plasma layer. Figure 14 shows *in vitro* blood (~20% Hct in PS) through the rectangular PDMS microchannel, for two different flow rates. The results illustrate that the RBCs flowing in this particular microchannel (300 μm wide, 45 μm deep) have no tendency to migrate toward the center axis for a Re of up to 0.1.

We next investigated the effect of the suspension fluid. In Fig. 15, we show human RBCs (~20% Hct) suspended in dextran 40 (Dx-40, Otsuka Medicine, Japan) for Re values up to 0.08. Using this high-molecular-weight suspension fluid, we eliminated the effects of sedimentation of the RBCs at low shear rates. The qualitative results from Fig. 15 also show no tendency for the RBCs to undergo axial migration.

Finally, we investigated the flow behavior of RBCs (~20% Hct) suspended in Dx-40 through a smaller PDMS microchannel (100 μm wide, 62 μm deep), for a Re of ~0.03 (see Fig. 16). In contrast to the previous results, the RBCs flowing through this PDMS microchannel had a tendency to migrate toward the microchannel axis, promoting the formation of a plasma layer. Although we do not have extensive data on the influence of the width, it is nevertheless clear that the formation of the plasma layer is enhanced as the width becomes narrower.

4 Discussion

4.1 Flow behavior of PS and *in vitro* blood through a PDMS microchannel

In the present study, we determined the velocity profiles of PS fluid and *in vitro* blood (20% Hct) in a rectangular PDMS microchannel with a low aspect ratio (h/w = 0.15) using a confocal micro-PIV system. In the case of PS fluid, our results were in good agreement with the analytical solution around the central plane (z = 17.5 μm, z = 22.5 μm, and z = 27.5 μm). However, at locations closer to the wall, the errors were slightly larger than 7%. We believe that these larger errors were primarily attributable to "second-order effects," such as the surface roughness of the wall and background noise generated from particles adhering on the wall (bias effect). Although it is important to consider the data from all planes, we believe that the best results from the confocal system were presented in the middle plane. These results also demonstrated that around the central region, PS velocity profiles were markedly blunt, which is consistent with the characteristic behavior of a Newtonian fluid through a rectangular microchannel with a low aspect ratio.

By comparing the averaged ensemble velocity profiles of PS fluid and *in vitro* blood flow, we observed small deviations at all optically sectioned planes. These deviations were found to be larger at locations closer to the wall. Furthermore, the ensemble velocity profiles at the central

plane for the *in vitro* blood were not characterized by a flat profile in the central region; rather, the profile had small perturbations. The reasons for these small perturbations are still not completely understood. However, from the visualization of the RBCs' motion through the rectangular microchannel, interactions between neighboring RBCs seem to be an important factor to take into account. The abrupt increase in the shear rate in the vicinity of the wall likely plays an important role in the local disturbance effects caused by both rotational and tumbling motion of deformable RBCs within the fluid flow. Moreover, temporal variation in the hematocrit could be another factor contributing to the perturbations described above. From the six measurements (Fig. 12 shows two of six) performed at the center plane at different time periods, all showed random perturbations on the averaged ensemble velocity profiles. This suggests that the transverse motion of the RBCs fluctuates over time, consequently affecting the local apparent viscosity of the fluid. Effects such as Brownian motion, microelectrohydrodynamics, and bottlenecks (Tabeling 2001; Nguyen and Wereley 2002) seem unlikely to contribute significantly to the perturbations found in the *in vitro* blood velocity profiles because such perturbations were small when compared to the PS fluid profiles measured under the same experimental conditions. The present results suggest that the presence of deformable RBCs suspended within the plasma flow plays an important role on the hydrodynamic disturbance effect seen on the *in vitro* blood velocity profiles. These observations are consistent with several other measurements performed in glass microchannels (Goldsmith and Turitto 1986; Alonso et al. 1995; Lima et al. 2007). Further studies to clarify the presence of these fluctuations on the ensemble velocity profiles need to be conducted, not only using microchannels that closely mimic actual human microvessels, but also using higher resolution objective lenses.

4.2 Plasma layer in a straight PDMS microchannel

It is well known that RBCs in microvessels less than 300μm wide (Fahraeus and Lindqvist 1931; Chien et al. 1984; Pries and Secomb 2003) tend to migrate toward the axis, pro-

Table 2 Major advantages of PDMS microchannels over glass capillaries

Physicochemical factors that affect blood flow behavior	Glass capillaries	PDMS microchannels	Comments
Ability to culture endothelial cells near to confluence	Complex in closed microchannels	Possible	Recently techniques have been developed to culture endothelial cells near to confluence in PDMS microchannels[a,b,c]. To our knowledge, no work has reported culture cells near to confluence in closed glass microchannels. This is only possible by using parallel plate flow chambers[d].
Mechanical properties, ultimate tensile stress (UTS), Young's elastic modulus (E)	Rigid material (UTS ~300 to 900 MPa[e], E ~70 Gpa[e])	Flexible material (UTS ~3.9 to 10.8 MPa[f], E ~0.75 MPa[g])	PDMS microchannels may be able to mimic the deformability of *in vivo* microvessels (UTS ~0.4 to 1.4 MPa[h], E ~2.5 MPa[i]). PDMS allows large deflections with small actuation forces[g].
Geometry of the flow channel	Any kind of geometry using photolithography, but limited in cross section, especially aspect ratio	Any kind of geometry	Presently, it has become possible to fabricate rectangular PDMS microchannels with complex geometries[j,k]. Fabrication of microchannels in PDMS is simple, rapid, and has high replication fidelity. In contrast, fabrication in glass increases the time, complexity, and cost of the fabrication process[l].

[a] Borenstein et al. 2002
[b] Shin et al. 2004
[c] Kaji et al. 2006
[d] Brown 2000
[e] Rika nenpyo 1996
[f] Mata et al. 2005
[g] Unger et al. 2000
[h] Holzapfel et al. 2005
[i] Steiger et al. 1989
[j] Shevkoplyas et al. 2003
[k] Lima 2007
[l] McDonald and Whitesides 2002.

moting the formation of a plasma layer adjacent to the vascular walls. In the present study, we used a PDMS microchannel with a width of 300 μm and depth 45 μm. For this particular microchannel, no plasma layer was observed during our experiments. To clarify the formation of the plasma layer in PDMS microchannels, we investigated the effect of different parameters on the formation of the plasma layer, including geometry, flow rate, and suspending media. Under similar conditions, our results showed that for a 300-μm-wide microchannel, no plasma layer was formed, whereas for a 100 μm width, a thin plasma layer was clearly observed. Thus, our qualitative results indicate that the geometry of PDMS microchannel is primarily responsible for the formation of the plasma layer. In addition, our results indicate that the plasma layer is enhanced as the width becomes narrower. This finding is consistent with a recent study on the flow of RBCs in model constrictions (Faivre et al. 2006).

4.3 PDMS versus glass microchannels

Several studies on blood flow in glass microchannels and in microvessels have yielded conflicting results with respect to flow resistance and deformability of RBCs (Pries et al. 1994; Suzuki et al. 1996). However, the observed *in vivo/in vitro* discrepancies have not yet been convincingly explained. One way to overcome the limitations of glass capillaries is the use of PDMS microchannels. PDMS microchannels differ from glass capillaries in several ways (see Table 2):

1. The permeability to gases, such as oxygen, is a unique advantage culturing living endothelial cells near to confluence (Borenstein et al. 2002; Shin et al. 2004) in closed microchannels, a task extremely difficult to achieve in glass capillaries. Recently, a cellular micropatterning technique based on an electrochemical method (Kaji et al. 2006) was used successfully to culture endothelial cells on the surfaces of PDMS microchannels;
2. PDMS is an elastomeric and biocompatible material. The typical ultimate tensile stress (UTS) for PDMS ranges from 3.9 to 10.8 MPa (Mata et al. 2005), whereas the Young's elastic modulus (E) has a value of ~0.75 MPa (Unger et al. 2000). The UTS and E of blood vessels have values from 0.4 to 1.4 MPa (Holzapfel et al. 2005) and ~2.5 MPa (Steiger et al. 1989), respectively. The UTS and E are PDMS-formulation-dependent. PDMS may be able to more closely mimic the geometric and structural properties of *in vivo* microvessels by adjusting the ratio of the cross-linker (curing agent) and the thickness of the wall;
3. Using PDMS, it is easy to replicate complex microvascular networks with submicron fidelity (McDonald et al. 2002; Shevkoplyas et al. 2003; Shin et al. 2004; Lima 2007);
4. Due to its spontaneous adhesion onto glass substrates, PDMS sealing does not need any complex bonding technique. Thus, PDMS microchannels in addition to offering optimum optical access for confocal systems can be reused several times because of its reversible bonding. Glass-to-glass sealing requires elaborate bonding processes, such as direct, thermal compression, or hydrofluoric bonding methods, which are time-consuming and need very careful processing to obtain an acceptable yield. Using bonding interlayers, such as silicon for anodic bonding, metal for fusion or eutectic bonding, and spin-on-glass for thermal compression bonding are other options; however, the interlayer also tends to be deposited in the microchannel. In addition, all of these bonding methods need flat, smooth, and clean surfaces, which require a clean room facility.
5. It is possible to integrate several functional components, such as heaters, micromixers, micropumps, microvalves, and temperature and pressure sensors into a PDMS device (Fujii 2002; Thorsen et al. 2002).
6. No need exists to use a refractive-index-matching liquid to minimize refraction from the walls. As a result, it is possible to use high magnification objective lenses (40×, 60×, 100×) with high NA, which typically have a working distance from 100 to 200 μm. Consequently it is possible to obtain images with much higher resolution.

In addition, using a soft lithography technique, it is possible to easily fabricate precise and reproducible rectangular microchannels at low cost because the master mold is reusable. A rectangular PDMS microchannel with a low aspect ratio seems to be appropriate for performing confocal micro-PIV measurements of *in vitro* blood with Hcts close to the actual *in vivo* Hct in the microcirculation. However, this geometry may not reflect the actual physiology of the microcirculation. Hence, very recently we successfully fabricated straight circular PDMS microchannels using a wire-casting technique (Lima 2007). The fabrication of circular PDMS microchannels with complex geometries remains a challenge. Borenstein and his coworkers (Borenstein et al. 2002, Shin et al. 2004) are developing a precise alignment technique to produce true cylindrical channels. However, the alignment procedure is complex, time-consuming, and the thickness of the two matching PDMS templates containing the semicircular microchannels may limit its practical application with confocal systems.

Despite the limitations of PDMS microchannels, it is clear that this kind of microdevice exhibits features closer to actual physiological conditions than glass capillaries. Although PDMS microdevices are promising for mimicking the *in vivo* microvascular environment, many chal-

lenges remain. First, current PDMS fabrication processes need improvement to produce precise circular microchannels with thin walls less than 200 μm to obtain accurate measurements by means of confocal systems. Second, PDMS collapsible microchannels need to be developed to mimic the deformability of blood vessels more closely. Finally, it is also important to evaluate whether current cell culture techniques used in PDMS microchannels create a microvascular environment that is closely representative of the *in vivo* situation.

4.4 Ongoing development

The *in vitro* research performed with classical glass microchannels has revealed several phenomena that occur in the microcirculation. Some examples are the Fahraeus effect and Fahraeus–Lindqvist effect (Chien et al. 1984). However, several recent studies on flow resistance (Pries et al. 1994) and RBC deformation (Suzuki et al. 1996) have shown quantitative differences between the results in microvessels and in glass microchannels. The reason for these differences still remains unclear. Glass microchannels differ from microvessels in several respects, such as elasticity and geometry of the microchannel and biological effect by the endothelial inner surface. We believe that the limitations encountered in using glass microchannels can be overcome by employing a PDMS microchannel (see Table 2). Nevertheless, before moving to a more elaborate PDMS microchannel, we must first clarify the flow behavior of blood in terms of a simple geometry similar to the one used in the present study. To fully exploit the potential of this combined system, we are working to develop a biochip to mimic the *in vivo* environment. By using an innovative cellular micropatterning technique based on an electrochemical method (Kaji et al. 2006), we expect to culture endothelial cells on the surfaces of the PDMS microchannel to near confluence. In addition, by combining this microdevice with the confocal system, we will be able to identify and quantitatively measure cellular and molecular events occurring between the blood cells and endothelium. As a longer-range goal, we believe that this ongoing research will lead to new insights into complicated microcirculation phenomena, such as the role of the glycocalyx on the blood flow behavior and the thrombogenesis process.

Because of their outstanding properties, rectangular PDMS microchannels are gaining popularity in biomedical research. In addition to providing the ability to investigate a variety of phenomena in the microcirculation (Takayama et al. 1999; Fujii 2002; Shevkoplyas et al. 2003), this kind of microfluidic device may be useful as a "lab-on-a-chip," a clinical diagnostic instrument. However, until now, precise measurements of blood flow behavior through this kind of microchannel have not been performed. In the present study, we demonstrated that by combining the rectangular PDMS microchannel with a confocal micro-PIV system it is possible to obtain both qualitative and quantitative information about the complex biophysical behavior of *in vitro* blood flow at a mesoscopic level. Thus, we believe that the present combination has potential as a powerful tool to investigate several phenomena in the microcirculation.

5 Conclusions

We applied a confocal micro-PIV system to examine PS and *in vitro* blood flowing in a rectangular PDMS microchannel with a low aspect ratio. For PS, the flattening of the velocity profiles was in good agreement with an established analytical solution for this kind of microfluidic device. However, when we assessed the flow of *in vitro* blood (20% Hct), small fluctuations were observed in the velocity profiles at optically sectioned planes along the z-axis. Blood flow measurements performed at the center plane of the microchannel clearly show small fluctuations on averaged ensemble velocity profiles. The reasons for the encountered "microturbulences" are not entirely clear, but our qualitative observations indicate that interactions between neighboring RBCs, the high shear rate generated in the vicinity of the walls, and temporal fluctuations in the hematocrit may play important roles in the hydrodynamic disturbance effects encountered in the blood velocity profiles. However, due to the variety of complex phenomena occurring at the microscale level, further studies are needed to clarify the presence of these fluctuations on the ensemble velocity profiles.

The measurements presented in this study clearly showed that confocal micro-PIV can be effectively integrated with a PDMS microchannel to obtain blood velocity profiles along the full depth of the microchannel because of its 3-D optical sectioning capability. This study also demonstrated that the combination of confocal micro-PIV systems with PDMS microchannels can play an important role in not only assessing existing theories, models, and computer simulations of the microcirculation, but also in the development of a more accurate biochip device for various biomedical applications, such as patient diagnosis and monitoring, drug delivery, and cancer cell detection.

Acknowledgements This study was supported in part by the following grants: International Doctoral Program in Engineering from the Ministry of Education, Culture, Sports, Science and Technology of Japan (MEXT), "Revolutionary Simulation Software (RSS21)" next-generation IT program of MEXT; Grants-in-Aid for Scientific Research from MEXT and JSPS Scientific Research in Priority Areas (768) "Biomechanics at Micro- and Nanoscale Levels," Scientific Research (A) No.16200031 "Mechanism of the formation, destruction, and movement of thrombi responsible for ischemia of vital organs".

The authors also thank all members of Esashi, Ono and Tanaka Lab. for their assistance in fabricating the PDMS microchannel.

References

R. Adrian, Annu. Rev. Fluid Mech. **23**, 261–304 (1991)

C. Alonso, A. Pries, O. Kiesslich, D. Lerche, P. Gaehtgens, Am. J. Physiol. **268**(1 Pt 2), H25–H32 (1995)

M. Baker, H. Wayland, Microvasc. Res. **7**, 131–143 (1974)

D. Beebe, G. Mensing, G. Walker, Annu. Rev. Biomed. Eng. **4**, 261–286 (2002)

L. Bitsch, L. Olesen, C. Westergaard, H. Bruus, H. Klank, J. Kutter, Exp. Fluids **39**, 505–511 (2005)

J. Borenstein, H. Terai, K. King, E. Weinberg, M. Kaazempur-Mofrad, J. Vacanti, Biomedical Microdevices **4**(3), 167–175 (2002)

G. Born, A. Melling, J. Whitelaw, Biorheology **15**, 163–172 (1978)

T. Brown, J. Biomech. **33**, 3–14 (2000)

H. Bruus, *Theoretical microfluidics* (MIC, Technical University of Denmark, Denmark, 2004)

G. Bugliarello, J. Hayden, Trans. Soc. Rheol. **7**, 209–230 (1963)

C. Caro, T. Pedley, R. Schroter, W. Seed, *The mechanics of the circulation* (Oxford University Press, 1978)

W. Chang, D. Akin, M. Sedlak, M. Ladisch, R. Bashir, Biomedical Microdevices **5**(4), 281–290 (2003)

S. Chien, S. Usami, R. Skalak, *Blood flow in small tubes Handbook of Physiology – The cardiovascular system IV* (1984) 217–249

T. Cochrane, J. Earnshaw, A. Love, Med. Biol. Eng. Comput. **19**, 589–596 (1981)

C. Duffy, J. McDonald, O. Schueller, G. Whitesides, Anal. Chem. **70**, 4974–4984 (1998)

S. Einav, R. Berman, P. Fuhro, P. DiGiovanni, S. Fine, J. Fridman, Biorheology **12**, 207–210 (1975)

R. Fahraeus, T. Lindqvist, Am. J. Physiol. **96**, 562–568 (1931)

M. Faivre, M. Abkarian, K. Bickraj, H. Stone, Biorheology **43**, 147–159 (2006)

T. Fujii, Microelectron. Eng. **61–62**, 907–914 (2002)

P. Gaehtgens, Biorheology **24**, 367–376 (1987)

P. Gaehtgens, H. Meiselman, H. Wayland, Microvasc. Res. **2**, 13–23 (1970)

S. Gifford, M. Frank, J. Derganc, C. Gabel, R. Austin, T. Yoshida, W. Bitensky, Biophys. J. **84**, 623–633 (2003)

H. Goldsmith, V. Turitto, Tromb. Haemost. **55**, 415–435 (1986)

H. Golster, M. Linden, S. Bertuglia, A. Colantuoni, G. Nilsson, F. Sjoberg, Microvasc. Res. **58**, 62–73 (1999)

R. Gomez, R. Bashir, A. Sarikaya, M. Ladish, J. Sturgis, J. Robison, T. Geng, A. Bhunia, H. Apple, S. Wereley, Biomedical Microdevices **3**(3), 201–209 (2001)

G. Holzapfel, G. Sommer, C. Gasser, P. Regitnig, Am. J. Physiol Heart Circ. Physiol. **289**, H2048–H2058 (2005)

H. Kaji, T. Kawashima, M. Nishizawa, Langmuir **22**, 10784–10787 (2006)

G.B. Kim, S.J. Lee, Exp Fluids **41**, 195–200 (2006)

H. Kinoshita, M. Oshima, S. Kaneda, T. Fujii, Proceedings of the 9thICMSCLS (Boston, Massachusetts, USA, 2005)

A. Koutsiaris, D. Mathioulakis, S. Tsangaris, Meas. Sci. Technol. **10**, 1037–1046 (1999)

R. Lima, Analysis of the blood flow behavior through microchannels by confocal micro-PIV/PTV system, Doctoral thesis (Tohoku University, Japan, 2007)

R. Lima, S. Wada, K. Tsubota, T. Yamaguchi, Proceedings of the 3rd IASTED ICB—BioMech (Benidorm, Spain, 485, 2005)

R. Lima, S. Wada, K. Tsubota, T. Yamaguchi, Meas. Sci. Technol. **17**, 797–808 (2006)

R. Lima, S. Wada, M. Takeda, K. Tsubota, T. Yamaguchi, J. Biomech. **40**, 2752–2757 (2007)

N. Maeda, Jpn. J. Physiol **46**, 1–14 (1996)

A. Mata, A. Fleischman, S. Roy, Biomedical Microdevices **7**(4), 281–293 (2005)

J. McDonald, G. Whitesides, Acc. Chem. Res **35**(7), 491–499 (2002)

G. Mchedlishvili, N. Maeda, Jpn. J. Physiol **51**, 19–30 (2001)

C. Meinhart, S. Wereley, J. Santiago, J. Fluids Eng **122**, 285–289 (2000)

G. Minas, J. Martins, J. Ribeiro, R. Wolffenbuttel, J. Correia, Sens. Actuators **110**, 33–38 (2004)

J. Moger, S. Matcher, C. Winlove, A. Shore, J. Biomed. Opt. **9**(5), 982–994 (2004)

N. Mortensen, F. Okkels, H. Bruus, Phys. Rev. E **71**, 1–4 (2005)

A. Nakano, Y. Sugii, M. Minamiyama, H. Niimi, Clin. Hemorheol. Microcirc. **29**, 445–455 (2003)

N. Nguyen, S. Wereley, *Fundamentals and applications of microfluidics* (Artech House, Inc., Norwood, MA, 2002)

J. Park, K. Kihm, Opt. Lasers Eng. **44**, 208–223 (2006)

J. Park, C. Choi, K. Kihm, Exp. Fluids **37**, 105–119 (2004)

A. Parthasarathi, S. Japee, R. Pittman, Ann Biomed. Eng. **27**, 313–325 (1999)

A. Pries, T. Secomb, Clin. Hemorheol. Microcirc. **29**, 143–148 (2003)

A. Pries, T. Secomb, T. Gessner, M. Sperandio, J. Gross, P. Gaehtgens, Circ. Res. **75**, 904–915 (1994)

M. Raffel, C. Willert, J. Kompenhans, *Particle image velocimetry: a practical guide* (Springer, Germany, 1998)

Rika nenpyo, Chronological scientific tables, (National Astronomical Observatory), Maruzen Co., Japan, 1996

J. Santiago, S. Wereley, C. Meinhart, D. Beebe, R. Adrian, Exp Fluids **25**, 316–319 (1998)

T. Secomb, Symp. Soc. Exp. Biol. vol 49 (London, UK, 1995), pp. 305–321

S. Shevkoplyas, S. Gifford, T. Yoshida, M. Bitensky, Microvasc. Res. **65**, 132–136 (2003)

M. Shin, K. Matsuda, O. Ishii, H. Terai, M. Kaazempur-Mofrad, J. Borenstein, M. Detmar, J. Vacanti, Biomedical Microdevices **6** (4), 269–278 (2004)

H. Steiger, R. Aaslid, S. Keller, H. Reulen, Heart Vessels **5**(1), 41–46 (1989)

N. Sutton, M. Tracey, I. Johnston, R. Greenaway, M. Rampling, Microvasc. Res. **53**, 272–281 (1997)

Y. Suzuki, N. Tateishi, M. Soutani, N. Maeda, Microcirculation **3**, 49–57 (1996)

P. Tabeling, Proceedings of the 14th Australasian Fluid Mechanics Conference (Adelaide, Australia, 2001)

S. Takayama, J. McDonald, E. Ostuni, M. Liang, P. Kenis, F. Ismagilov, G. Whitesides, Patterning cells and their environments using multiple laminar fluid flows in capillary networks Proc. Natl. Acad. Sci. **96**, 5545–5548 (1999)

T. Tanaani, S. Otsuki, N. Tomosada, Y. Kosugi, M. Shimizu, H. Ishida, Appl. Opt. **41**(22), 4704–4708 (2002)

G. Tangelder, D. Slaaf, M. Muijtjens, T. Arts, M. Egbrink, R. Reneman, Circ. Res. **59**, 505–514 (1986)

T. Thorsen, S. Maerkl, S. Quake, Science **298**, 580–584 (2002)

M. Toner, D. Irimia, Annu. Rev. Biomed. Eng. **7**, 77–103 (2005)

K. Tsukada, H. Minamitami, E. Sekizuka, C. Oshio, Physiol. Meas. **21** (4), 459–471 (2000)

W. Uijttewaal, E. Nijhof, R. Heethaar, J. Biomech. **27**, 35–42 (1994)

M. Unger, H. Chou, T. Thorsen, A. Scherer, S. Quake, Science **288**, 113–116 (2000)

P. Vennemann, K. Kiger, R. Lindken, B. Groenendijk, S. Stekelenburg-de Vos, T. Hagen, N. Ursem, R. Poelmann, J. Westerweel, B. Hierk, J. Biomech. **39**, 1191–1200 (2006)

S. Wilhelm, B. Grobler, M. Gluch, H. Heinz, *Confocal laser scanning microscopy: principles* (Carl Zeiss, Germany, 2003)

C. Willert, M. Raffel, J. Kompenhans, B. Stasicki, C. Kahler, Flow Meas. Instrum. **7**, 247–256 (1996)

Journal of
Nanoscience and Nanotechnology
Vol. 8, 1–8, 2008

Ultra-Stable Nanoparticles in $A_{II}B_{VI}$ (A_{II} = Cd, Zn; B_{VI} = S, Se, Te) Compounds

V. R. Romanyuk[1, †, *], I. M. Dmitruk[1, ‡], Yu. A. Barnakov[1], R. V. Belosludov[2], and A. Kasuya[1]

[1] *Center for Interdisciplinary Research, Tohoku University, Sendai, 980-8578, Japan*
[2] *Institute for Materials Research, Tohoku University, Sendai, 980-8577, Japan*

Laser ablation on binary $A_{II}B_{VI}$ compounds exhibits in time-of-flight mass spectra abundant peaks at stoichiometric $(A_{II}B_{VI})_n$ with $n = 13$, 19, 33 and 34 measured on bulk powders of CdSe, CdS, CdTe, ZnS and ZnSe. Investigation on solution grown nanometer size particles of CdSe shown an existence of ultra-stable stoichiometric clusters $(CdSe)_{13}$, $(CdSe)_{19}$, $(CdSe)_{33}$, $(CdSe)_{34}$ and $(CdSe)_{48}$. This set of n has not been predicted as particularly stable particles in previous bulk fragment models based on either zinc-blende or wurtzite, and a different type of structures is required to explain our experimental results. Present investigation shows that nanoparticles formed in vacuum as magic numbers above are found in solution as preferentially grown species in CdSe, and possibly in other $A_{II}B_{VI}$. It is suggested that the high stability of the observed magic clusters originates from their specific structure as endohedral binary fullerenes, supposedly. These molecular-like particles composed of few tens of atoms lie between atom and solid, and exhibit novel materials functions not realizable in the bulk.

Keywords: II–VI Compound Nanoparticles, Mass Spectra, Magic Numbers, Endohedral Structure, Closed Shell.

RESEARCH ARTICLE

1. INTRODUCTION

Nanostructured materials attract much of our attention as an intermediate phase between molecule and solid to explore fundamental aspects and possible applications in nano-electronic, biomedical and catalytic devices. Their extremely strong size and shape dependent structures in atomic scale[1–4] may lead to functional properties not realized in other forms of condensed matter. Nanoparticles of semiconductors have been particularly studied during the last decade in binary II–VI compounds,[5,6] CdS,[7–10] CdSe[2,3,11,12] and CdTe,[13–15] and their core–shell combinations with III–V, InAs/CdSe and InAs/InP,[16] because of recent advances in preparing high quality samples in solution. These nanoparticles, however, are mostly grown in diameters larger than 2 nm, and their structures are essentially of the bulk.

Particles of less than 1 nm are prepared more readily in vapor produced by thermal evaporation or laser ablation in vacuum. Martin[1] shows in his extensive mass spectral analysis, especially in metallic elements that small particles may have structures characterized by a concept of shell periodicity that is entirely different from the translational ones in bulk crystals. Similarly to shell structures in atoms and nuclei, the particle becomes particularly stable at the number of constituent atoms/molecules, n, that coincides with values called magic number to close the periodic shell. In mass spectra, stable magic number particles appear as abundant peaks relative to those of neighboring masses. The observed spectra further show that this shell periodicity exhibits a transition from "shells of electrons" to "shells of atoms." In Na_n, for example, this transition is noted at $n \sim 1{,}500$ as a discontinuity in periodicity represented by the sequence of magic numbers. It occurs because the origin to determine the stability of particle switches from the electronic state for $n < 1{,}500$, to the atomic arrangement for $n > 1{,}500$. The stable structures in both sides are still symmetrically different from the bulk of translational periodicity appearing at much larger sizes.[1,17]

Comparing with metals, very few works have been reported on nanoparticles in semiconductor compounds with $n > 20$ partly because of difficulty in obtaining high yield of vapor to condense into larger particles. Previous works in ZnS as a binary $A_{II}B_{VI}$ compound (A_{II} = Cd, Zn; B_{VI} = S, Se, Te) find stoichiometric $(ZnS)_n$ that are

*Author to whom correspondence should be addressed.
†Present address: Institute for Physics of Semiconductors NAS of Ukraine, Prospect Nauki 41, Kyiv, 03028 Ukraine.
‡Permanent address: Physics Department, Kyiv Taras Shevchenko University, Kyiv, 03127 Ukraine.

1533-4880/2008/8/001/008 doi:10.1166/jnn.2008.433

abundant in $n < 35$.[1, 18] Other binary systems of smaller ones are extensively studied, including Al_nS_m (Ref. [19]) and Tc_nS_m.[20]

Small systems have much more freedom and flexibility than the bulk solid to adopt structures that would lower their free energy by changing dimensionality and morphology with atomic arrangements not possible in crystals.[3, 6, 21] Calculation on BN by Seifert,[22] for example, predicts that cage-like polyhedral shells consisting of 4- and 6-membered rings of alternately connected -B-N- are stable as stoichiometric closed networks in $(BN)_n$. Magic numbers are determined as $n = 12, 16, 28, 36 \ldots$. Pokropivny[23] also proposed 8-membered rings in addition to 4- and 6-. Experimentally $(BN)_n$ in polyhedral structure of ~1 nm was observed in electron microscope[24] and by mass spectrometry.[25]

Recent extensive calculations[21, 26, 27] reveal more possibilities of polyhedrons not only in the form of a hollow shell but also those placing atoms/molecules in the center or around the shell for increasing stability and/or functionality. To search such nanoparticles experimentally, the mass measurement should be extended to larger particles over 1 nm in condensed vapor method and analyze magic number distributions in detail. Concurrently, these samples should be synthesized and tired to extract stable ones in macroscopic quantity for the purpose of identification and precise analyses. Our recent investigation in CdSe (Ref. [28]) followed this approach and finds magic number of $(CdSe)_n$ with $n = 13$, 19, 33 and 34 in the mass analysis of both vapor and solution grown samples. It also finds $(CdSe)_{13}$ and $(CdSe)_{34}$ as stable nanoparticles preferentially grown in atomic precision as identified in sharp excitonic peak at 415 nm in the optical absorption spectrum in solution.

In this paper we present results of time-of-flight mass spectroscopy (TOF-MS) of heteroatomic nanoclusters with tens of atoms which form in the plasma plume produced in vacuum by laser ablation of powders for some of the $A_{II}B_{VI}$ compounds. Our experimental results for the mentioned size range demonstrate that nanoclusters with $n = 13$, 33 and 34 for $(CdSe)_n$, $(CdS)_n$, $(CdTe)_n$, $(ZnSe)_n$, $(ZnS)_n$, $(ZnTe)_n$ possess unique stability. These nanoclusters are the first reliably identified ultra-stable stoichiometric II–VI compound nanoclusters. Besides that it was found that $(CdSe)_{48}$ is a next stable nanoparticle preferentially grown in solution. Thus, presented experimental data demonstrate that in the transition range of sizes from atoms to bulk fragments, there is exceptional stability for clusters with stoichiometric Cd:Se ratio as 1:1 and numbers of CdSe molecules 13, 33, 34, and 48. A possible explanation of their elevated stability is specific structure different from the bulk one.

Such molecular particles extractable from solution may be quite stable against coalescence to each other or reaction with others in contact and called "ultra-stable" compared with magic number particles detected in vacuum that are relatively stable under isolated environments. Ultra-stable nanoparticles are particularly suited as functional blocks for assembling into a variety of nanostructures.

2. SAMPLE PREPARATION AND MEASUREMENT DETAILS

Bulk samples used in our measurement were 99.99% pure powders of crystalline CdSe from Wako Pure Chemical Industries, Ltd., CdS, CdTe, ZnS, ZnTe and ZnSe–from Sigma-Aldrich, Co. A small amount of powder was pestled well in an agate mortar and then mixed with 0.5 ml of hexane. A portion of 1 μl was pipetted on a stainless steel target plate. After dried quickly, the plate with the sample was transferred to the mass spectrometer.

In addition, nanoparticles of CdSe were prepared in reverse micelles using decylamine as surfactant in toluene as described in Ref. [28]. Optical absorbance were measured on colloidal toluene solution of CdSe nanoparticles in 10 mm quartz cuvette with a Hitachi U-2000 spectrophotometer at room temperature.

All time-of-flight mass measurements were carried out using a Bruker Reflex III-T mass spectrometer equipped with a nitrogen laser of 337.1 nm wavelength, 0.5 mJ energy, 4 ns pulse width and 1 Hz repetition rate. Mass spectra were obtained for positively charged ions in linear mode without injecting cooling gas to the vaporizing source. Spectra for negative ions were similar but in low signal to noise ratios. Each spectrum is recorded by accumulating a total of about 500 laser shots on different points on the target source.

3. RESULTS AND DISCUSSION

3.1. Mass Spectra on Bulk Powders of $A_{II}B_{VI}$ Compounds

Figure 1(a) displays the time-of-flight mass spectrum of nanoparticles produced by laser ablation on powder of bulk wurtzite CdSe. It represents a typical distribution of high intensities in low mass region below 2,000 a.m.u. (atomic mass unit) followed by a diminishing tail toward high mass because smaller mass particles are produced or survived as stable species with much higher probabilities than larger ones in a violent vaporizing process.[29] Dominant peaks found are stoichiometric $(CdSe)_n$ spaced by 191.4 a.m.u. (=mass of Cd + Se) with prominent ones at $n = 13$, 33, 34, and less prominent at $n = 19$ that exhibit intensities notably higher than their immediate neighbors. These prominent peaks, recognized by magic numbers, may correspond to a set of particularly stable chemical species realized in their specific structure just at these numbers of n. Since our measurements use no cooling gas during laser ablation, abundantly observed high mass particles must be extremely stable ones. The mass numbers, however, are quite unexpected from any set or series known

RESEARCH ARTICLE

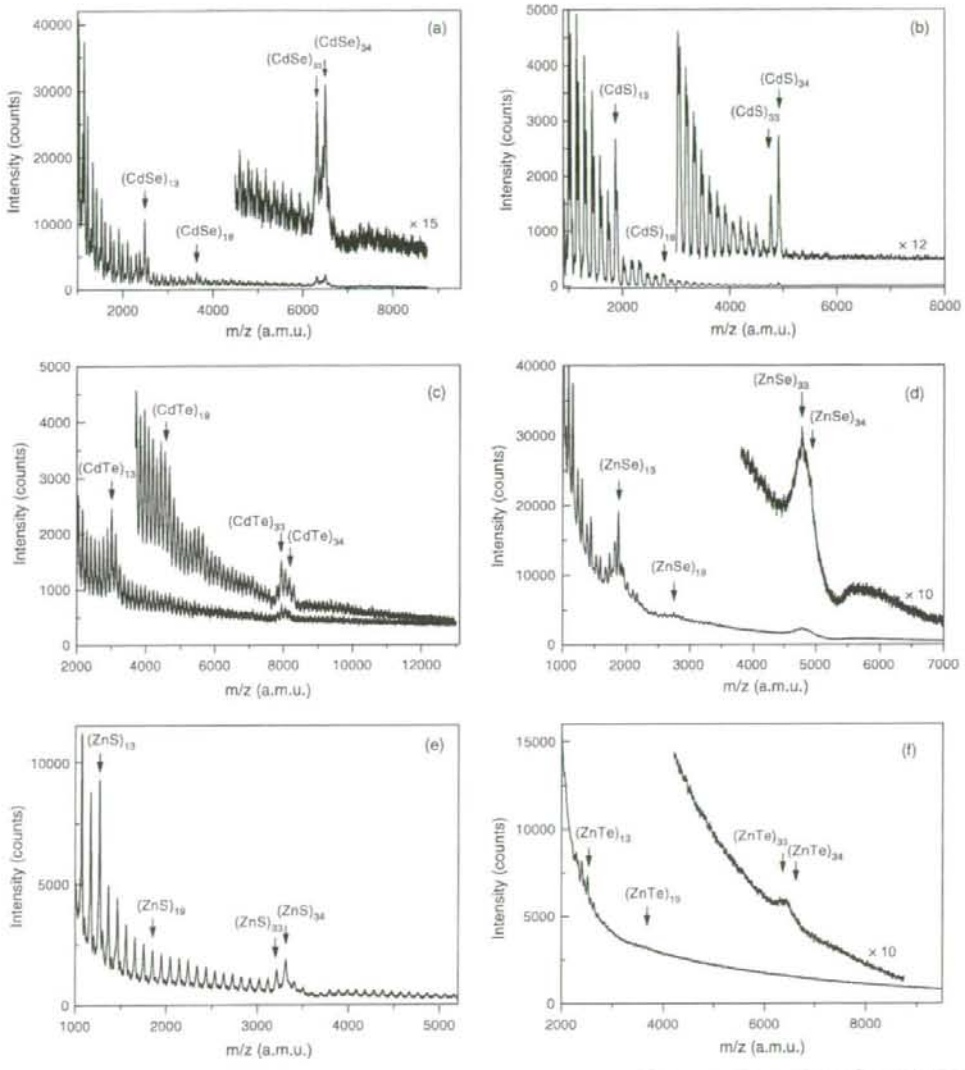

Fig. 1. Mass-spectra of $A_{II}B_{VI}$ nanoparticles formed in laser ablation of crystalline powders of CdSe (a), CdS (b), CdTe (c), ZnSe (d), ZnS (e), ZnTe (f). For some compounds the spectra near $n = 33, 34$ are expanded in intensity scale.

in the past. The peculiar feature lies after $n = 19$ that two consecutive number peaks appear sharply at $n = 33$ and 34 with distinctively high intensities of nearly equal magnitudes and contrastingly, the rest of all neighboring peaks are diminishingly small evenly. This behavior is hard to realize in bulk fragment models based on zinc-blende or wurtzite crystal in $A_{II}B_{VI}$ compounds.[1,18] Because of an open structure, the stability of fragment would not depend drastically on n, and cannot be equally so high particularly at two consecutive number particles and equally so low for all others in a wide range from their immediate neighbors.

The above spectral features are found common in other $A_{II}B_{VI}$ compounds, CdS, CdTe, ZnSe, ZnS and ZnTe, as shown in Figures 1(b)–(f), respectively. All show prominent peaks at $n = 33$ and 34, though details are different. Among them, CdSe exhibits the highest intensity ratio of

these two peaks to diminishingly weak neighbors in a wide mass range. This ratio is still high in CdS and ZnS with respect to higher masses but not so much for lower. In CdTe, ZnSe and ZnTe, neighbors on both sides exhibit rather high intensities. In ZnSe and ZnTe, each mass peak becomes broader and overlapping partly because higher laser intensity is necessary to obtain these spectra. Considerable fragmentation is evident especially towards low masses. At the highest laser intensity, a group of peaks appear near $n = 23$ in the measurement tuned for high mass region, as seen in the upper curve of Figure 1(c) on CdTe.

The intensity ratio of stoichiometric peaks to non-stoichiometric is also distinctively different. It is quite high in CdSe, CdS and, ZnS, but nearly unity in CdTe. Non-stoichiometric peaks are almost absent in ZnS in the entire mass range, and also in CdS but in $n > 30$ only. Double peaks in $n < 30$ correspond to $(CdS)_n$ and non-stoichiometric Cd_nS_{n+1}. The intensity of $Cd_{n+1}S_n$ on the other hand is extremely week. In Figure 1(c) on CdTe, Cd_nTe_{n+1} and $Cd_{n+1}Te_n$ would overlap to each other because atomic masses of Cd and Te are comparable, and these peaks cannot be distinguished in the spectrum. All these detailed differences found in Figure 1 may be used to study the stability and structure of $(A_{II}B_{VI})_n$.

In ZnS, previous mass analyses[1, 18] show strong stoichiometric peaks including $n = 13$ and 34 but neighboring and non-stoichiometric peaks are also relatively strong. This spectral profile is different from Figure 1(e) probably because of the difference in vaporization conditions. Our measurement uses no cooling gas and detects stable ones more selectively.

3.2. $(CdSe)_{33, 34, 48}$ Nanoclusters Prepared in Solution

Figure 2(a) displays mass spectra of CdSe nanoparticles prepared in solution. Curve 1 shows peaks at $n = 33$ and 34 which are much more pronounced relative to neighboring peaks than in Figure 1(a) of the bulk powder. These two peaks are also sharper than in Figure 1(a) and their widths are explained by isotope distributions of natural Cd and Se. Furthermore, low mass peaks near $n = 13$ are much weaker compared with $n = 33$ and $n = 34$ than in Figure 1(a). These results indicate that the sample dried on the target plate contains $(CdSe)_{33}$ and $(CdSe)_{34}$ as the main species selectively grown in solution because of their extremely high stabilities among others. The incident laser energy in this measurement was less than half of the bulk in Figure 1(a). These ultra-stable particles, therefore, are gently evaporated from the target plate as original chemical species rather than formed and ejected under a violent laser ablation process observed in the bulk powder measurement. The absence of peaks from surfactant and solvent implies that they are not firmly attached to these nanoparticles. Raising laser energy tends to increase neighboring

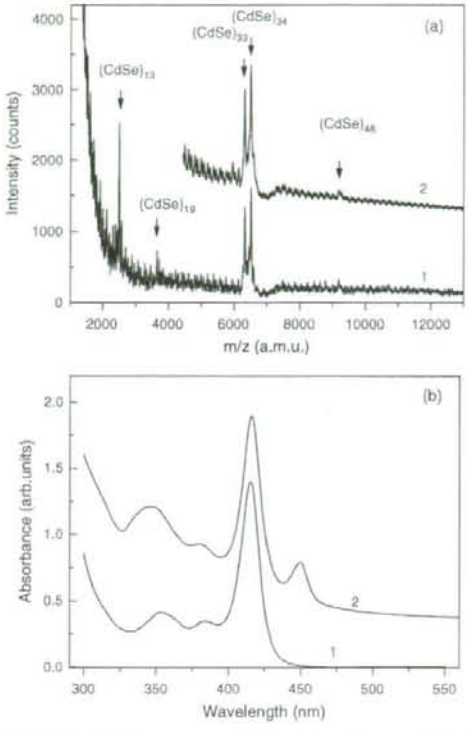

Fig. 2. Time-of-flight mass spectra (a) and absorption spectra (b) of CdSe nanoparticles grown by wet chemistry method in toluene for 1 day (curves 1) and for 13 days (curves 2).

peaks below $n = 33$ that accounted for by fragmentations of particles with $n = 33$ and 34 under laser excitation.

Curve 2 in Figure 2(a) displays a spectrum on the solution grown CdSe nanoparticles that are kept for 13 days at room temperature in toluene solution after synthesis. It shows $(CdSe)_{48}$ that is more pronounced than in Curve 1. This result indicates that $(CdSe)_{48}$ is also stable and selectively grown in solution during the aging period. Nanoparticles are surrounded by surfactants in reverse micelles that prevent from fast growth.

Curves 1 and 2 in Figure 2(b) correspond to optical absorption spectra of our samples in solution corresponding to Curves 1 and 2 in Figure 2(a), respectively. Curve 1 shows the main excitonic peak at 415 nm together with 382 nm and 352 nm. These peaks always show the same intensity ratios in our samples and belong to the same nanoparticle. Optical properties in CdSe nanoparticles of diameters larger than 1 nm have been studied extensively in Refs. [2, 3, 11, 30], and the main peak is found to blue shift as the diameter gets smaller by quantum confinement of electronic states in CdSe from 720 nm of the bulk

absorption edge. From the peak at 415 nm in Figure 2, the diameter is estimated as ~1.5 nm, in agreement with our AFM measurement on dried sample.[28] Based on the main peak position, diameter and mass analysis, the main species in solution are attributed to $(CdSe)_{33}$ and $(CdSe)_{34}$. If the bulk density is assumed, simple calculation shows that 1.5 nm of crystalline CdSe sphere contains about 30 Cd-Se pairs.

Curve 2 in Figure 2(b) shows the 415 nm peak slightly broader with a tail structure developed towards longer wavelength compared with Curve 1. In Figure 2(a) on the other hand, Curve 2 shows mass peaks above $n = 34$ slightly increased especially at $n = 48$ compared with Curve 1. These results indicate the growth of nanoparticles larger than $(CdSe)_{34}$ during the 13 day aging, and $(CdSe)_{48}$ may be another stable nanoparticle preferentially grown in solution.

Curve 1 in Figure 2(b) is quite similar to those reported previously on very small CdSe nanoparticles grown in different solution methods.[2, 11, 30–33] All incidentally show the sharp and strong main peak near 415 nm with almost identical overall spectral profiles, and the diameter is estimated as ~1.2 nm (Ref. [2]) and ~1.7 nm.[11] The peak width is in remarkable contrast to much broader ones typically observed above 450 nm on samples of larger diameters.[2, 3, 11] Our samples prepared at 80 °C and above exhibit a broad main peak centered at 480 nm and above.[28] These nanoparticles essentially have bulk crystalline structures and their stabilities do not depend sharply on diameter as expected from the open structure of bulk fragments. This is a main reason that they grow in wide diameter distributions in solution showing a broad peak. Samples in Figure 2 prepared at room temperature, on the other hand, show the same sharp and strong peak at 415 nm with nearly identical profile under a wide reaction conditions.

If a particle is made smaller and smaller down to 1 nm, the number of constituent atoms becomes less than a hundred and begins to play a decisive role in size and shape dependent stabilities that only those particles in a set of particular numbers become stable and grow preferentially in solution, resulting in discrete single-size distributions. Extremely sharp 415 nm peak and its observations in different methods of preparation[2, 11, 30–33] show the presence of this sharp selective process.

It looks a bit unusual that two ultra-stable clusters with $n = 33$ and $n = 34$ are so close. One can suppose that they are pieces of a parent cluster $(CdSe)_{67}$ broken in the mass-spectrometer. We paid special attention to look for it and also for clusters like $n = 46$, $n = 47$, $n = 80$, etc. But nothing was found in the large mass range except the weak peak of the $n = 48$ cluster mentioned above. Probably only these clusters have specific ultra-stable arrangements of atoms that are different from the bulk structure. Larger species have crystal-like zinc-blende or wurtzite structures with no precise stoichiometry and a size distribution of 5–15% as reported in Ref. [2]. Possible structures of stoichiometric ultra-stable clusters with $n \leq 48$ will be discussed below.

Mass spectra confirmed another unusual result obtained earlier in sample characterization. Energy disperse X-ray analysis gave the Cd:Se ratio as 1:1 within the accuracy of the instrument. It's hard to expect precise stoichiometry for such small clusters when even usually the crystalline semiconductor clusters demonstrate a deviation from stoichiometry when their sizes decrease.

3.3. Mass Spectra on Some $A_{III}B_{V}$ Compounds and Related Materials

The importance of stoichiometry in the stability of $A_{II}B_{VI}$ compounds is indicated in comparison with mass spectra of $A_{III}B_{V}$ (A_{III} = Ga, In; B_{V} = N, P, Sb, As) shown in Figures 3(a) on GaAs and 3(b) on InSb measured similarly to those in Figure 1. In both 3(a and b), the spectra show strong mass peaks that are only in the low mass region below 2,000 a.m.u. and far from 1:1 stoichiometry of A_{III} to B_{V} with no simple rule. In addition, no prominent peak appears near $(A_{III}B_{V})_{34}$, indicating no particularly stable nanoparticles in this mass range. Similar results are found in GaP and GaN. These spectra indicate that nanoparticles of $A_{III}B_{V}$ have stable structures quite different from $A_{II}B_{VI}$. Apparently, the stoichiometry is not the major factor governing the stability, in sharp contrast to $A_{I}B_{VII}$ of alkali-halide which is shown by previous mass spectroscopic analyses to be stable in 1:1 composition as small cuboids of the face-centered-cubic lattice.[1, 34] In these stable cuboids of ionic crystal, the charge is well balanced in atoms of both polarities connected alternately to each other in every direction along the lattice in a symmetric arrangement.

Such balance is difficult to achieve in the fragment of bulk $A_{III}B_{V}$ without some sort of reformation of the tetrahedral coordination. The directional and strong covalent bonds make this reformation energetically unfavorable at any number of constituent atoms and may leave the stability of bulk fragment rather size-insensitive, as seen in flat high mass distributions in Figures 3(a and b).

Because of the increasing ionicity and decreasing covalency from $A_{III}B_{V}$, nanoparticles of $A_{II}B_{VI}$ may be stabilized favorably by balancing the charge tightly in 1:1 stoichiometry with alternating network of A_{II} and B_{VI} in high symmetry reformed from the tetrahedral lattice fragment. Such energetically favorable rearrangements of atoms can be realized in small particles only at limited n's, as expected in our measurements.

Time-of-flight mass spectra with laser excitation depend so sensitively on the experimental condition of target vaporization and nanoparticle extraction from the vapor that measurements on different materials obtained with the same instrument are quite reliable and useful for detailed spectral analysis and comparison to find stable and useful

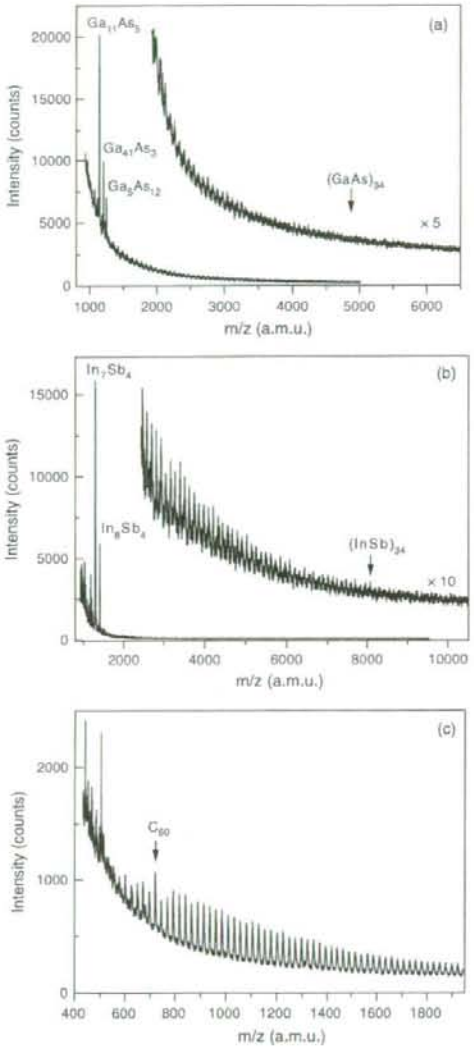

Fig. 3. Mass-spectra of $A_{III}B_V$ nanoparticles formed in laser ablation of crystalline powders of GaAs (a), InSb (b) and graphite (c).

nanoparticles. Figure 3(c) displays the result on graphite powder to show how stable $(A_{II}B_{VI})_{13}$, $(A_{II}B_{VI})_{33}$ and $(A_{II}B_{VI})_{34}$ are compared with their neighboring masses. It exhibits strong peak at C_{60} together with neighboring C_n of even n in comparable magnitudes in the tail of intense low mass peaks. The C_{60} peak is not particularly strong since no cooling gas is introduced on the vapor of C_n. The Figure 3(c) is in contrast with the prominent peaks of $(A_{II}B_{VI})_{33}$ and $(A_{II}B_{VI})_{34}$ also without cooling gas that show their extremely selective stabilities. Historically, the spectrum in laser ablation on graphite provided a decisive experimental fact to model the atomic arrangement of C_{60} (Ref. [35]) which is entirely different from bulk diamond or graphite. The experimental identification, however, had awaited its chemical synthesis five years later in macroscopic quantity[36] for the structural analysis in atomic precision. Our systematic measurement shows extremely selective stabilities of $(A_{II}B_{VI})_n$, and opens up the possibility to find more stable molecular-like particles extended from elemental carbon only to the vast variety of compound systems.

4. STRUCTURE OF ULTRA-STABLE $(A_{II}B_{VI})_n$ NANOCLUSTERS

The observation of ultra-stable clusters consisting of ten to hundreds of atoms assumes their specific structure. To date, published theoretical approaches applied to clusters of CdSe and related compounds in Refs. [1, 6, 37–39] considered them as fragments of bulk wurtzite or zinc-blende lattice with relaxed surface atoms but their calculations did not show agreement in ultra-stable compositions.

From the comparison of the mass spectra we can conclude that $n = 13$, 33 and 34 are magic numbers for ligand-free clusters for all the II–VI compounds studied here. Also, from our experiments with colloid solution we can conclude that $(CdSe)_{13}$, $(CdSe)_{33}$, $(CdSe)_{34}$ and $(CdSe)_{48}$ are ultra-stable clusters with ligand passivated surface. These numbers, especially for two consecutive 33 and 34 are difficult to explain consistently by open structures of compact crystalline fragments. The model by Martin[1] based on zinc-blende predicts $n = 13, 34, 70, 125, \ldots$, but not for 33 particularly. The basket model by Burnin[18] is presented only for $n = 13$.

The cage model by Seifert[22] in $(BN)_n$, on the other hand, has more possibility of explaining the stability.[28] The cage has a space at the center that can be filled by more atoms without affecting much the polyhedral morphology of closed structure. In more ionic compounds like $A_{II}B_{VI}$ compared with BN, polyhedrons are more stable by distributing atoms of both polarities alternately in the entire volume than only around the surface, especially in larger ones. Tetrahedral sp^3 bondings of these compounds are also favorable of three-dimensional distribution than sp^2 of two-dimensional. The model of $(BN)_n$ predicts magic numbers corresponding to closed empty cages as $n = 12, 16, 28, 36, \ldots$.

For binary compounds of normally 4-coordinated atoms, the probable building block is the 6-membered ring. And to have closed structure instead of plain sheet, some rings must be smaller ones–4-membered (5-membered rings observed in C_{60} and C_{70} are impossible for binary compounds with some ionicity). But we failed to construct symmetrical cage-like structure of $33 + 33$ or $34 + 34$

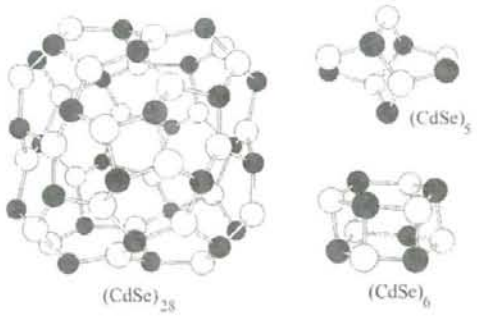

Fig. 4. Proposed structures for $(CdSe)_{33}$ and $(CdSe)_{34}$ clusters—empty $(CdSe)_{28}$ cage and internal patterns $(CdSe)_5$ and $(CdSe)_6$.

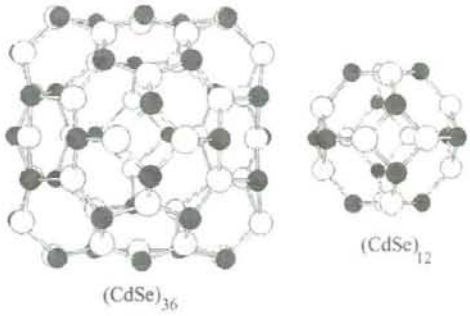

Fig. 5. Proposed structure for $(CdSe)_{48}$ cluster—outer cage $(CdSe)_{36}$ and internal cage $(CdSe)_{12}$.

atoms under these rules. The nearest high symmetry ball-like structure consists of 28 + 28 atoms and has 6 4-membered rings (Fig. 4). This contradiction can be resolved if we put inside another small pattern consisting of 5+5 or 6+6 atoms and composed also of 6-membered rings (Fig. 4). Its size matches well with the outer shell and the angular Cd atoms can form 3D bonds with the shell Se atoms (fourfold coordination). Saturation of the Cd atoms bonds partly decreases the dangling bonds number and reconstruction of the surface occurs (because more than 80% of atoms in particles are surface atoms). Stabilization of the clusters occurs by filling them inside with an additional network that acts as a core that is strongly interconnected to the outer cage. If we operate only with the experimental result from the mass spectrometry of the stoichiometric composition $(A_{II}B_{VI})_{34}$, then for the proposed cage-like structure with core $(CdSe)_6$ the number of dangling bonds is 56 (coordination number $N = 3.18$), while for the wurtzite bulk fragment proposed in Ref. [1] there are 62 dangling bonds and the coordination number $N = 3.09$ is lower. Typically, computer optimized cage-like structures have binding energies a few eV higher than bulk fragments.[28, 40] Saturation of bonds also causes the minimum of chemical reactivity. Maybe for the binary II–VI compounds it is essential to have a certain pattern inside the shell to keep it from collapse, and two possible internal patterns explain the two lines in the mass spectrum while in general the particles are very similar. The observation of stoichiometric nanoparticles is a strong indication that the charge balance is an important factor in determining the stability, and the detailed spectral differences in Figures 1(a) to (f) may be attributed partly to states of ionicity in these $A_{II}B_{VI}$ compounds. More experimental investigation is necessary for further analyses.

For the $(CdSe)_{48}$ cluster, a similar nested cage structure can be suggested. The nearest binary fullerene shell is at $n = 36$. Thus it has to incorporate $n = 12$ molecules. But that is exactly the composition of smallest shell (Fig. 5). Simple estimates of the difference of their diameters give a value which is very close to the Cd—Se bond length. It means that the $n = 12$ cage fits well into the $n = 36$ cage and that some atoms can form bonds between cages. Extensive first principle calculations[28] confirmed the high binding energies of the suggested structures of CdSe ultra-stable clusters.

5. CONCLUDING REMARKS

Time-of-flight mass analysis reveals that small particles of binary $A_{II}B_{VI}$ compounds are extremely stable in the stoichiometric form of $(A_{II}B_{VI})_n$ with $n = 13$, 19, 33 and 34, as observed abundantly over weak neighbors in laser ablation on bulk powders of CdSe, CdS, CdTe, ZnS, ZnSe. The remarkable stability of $(A_{II}B_{VI})_{33}$ and $(A_{II}B_{VI})_{34}$ is well demonstrated by the fact that massive particles of ~1 nm in diameter are produced selectively at only two specific mass numbers without intentionally cooling the vapor ejected in a violent ablation process in vacuum. This result has not been predicted in the past but is found common to all $A_{II}B_{VI}$ compounds measured in our simple experiment. These numbers and stoichiometry are particular to $A_{II}B_{VI}$ compounds and not to $A_{III}B_V$. The observed mass range lies in the gap between those of samples typically produced in vacuum and in solution, corresponding to the intermediate region between molecule and solid.

In cadmium selenide, $(CdSe)_{33}$, $(CdSe)_{34}$ and $(CdSe)_{48}$ are even found to grow preferentially in solution at room temperature by suppressing the formation of smaller and larger neighbors. This sharp selective stability enables us to obtain truly single-size stoichiometric nanoparticles in macroscopic quantity at precision expressed by the number of atoms instead of diameter.

Our experimental results show the presence of such ultra-stable nanoparticles of compounds having three-dimensional chemical bonds, like sp^3. These molecular nanoparticles are expected to have structures and properties uniquely specified by the number of constituent atoms. This specific structure must be different from the close

RESEARCH ARTICLE

packed arrangements of atoms in fragments of bulk crystals. One suggestion for structure of these clusters is a highly symmetric cage of binary fullerenes with a few additional atoms inside providing the stability of such heteroatomic compositions. These atomically well-defined materials not realized in the bulk serve as extremely useful functional units for basic studies in nanometer sciences and for a variety of device applications.

Acknowledgments: Authors would like to thank Dr. M. Kobayashi for helpful discussions and technical collaboration during mass-spectroscopy measurements. This work was supported in part by Grant-in-aid from the Ministry of Education in Japan.

References and Notes

1. T. P. Martin, *Phys. Reports* 273, 199 (**1996**); T. P. Martin, T. Bergmann, H. Gohlich, and T. Lamge, *J. Phys. Chem.* 95, 6421 (**1991**).
2. C. B. Murray, D. J. Norris, and M. G. Bawendi, *J. Am. Chem. Soc.* 115, 8706 (**1993**).
3. X. Peng, L. Manna, W. Yang, J. Wickham, E. Scher, A. Kadavanich, and A. P. Alivisatos, *Nature* 404, 59 (**2000**).
4. J. H. Adair, T. Li, T. Kido, K. Havey, J. Moon, J. Mecholsky, A. Morrone, D. R. Talham, M. H. Ludwig, and L. Wang, *Mater. Sci. Eng.* R23, 139 (**1998**).
5. M. C. Troparevsky and J. R. Chelikowsky, *J. Chem. Phys.* 114, 943 (**2001**).
6. P. Deglmann, R. Ahlrichs, and K. Tsereteli, *J. Chem. Phys.* 116, 1585 (**2002**).
7. T. Sugimoto, G. E. Dirige, and A. Muramatsu, *J. Coll. Interf. Sci.* 182, 444 (**1996**).
8. N. Pinna, K. Weiss, J. Urban, and M.-P. Pileni, *Adv. Mater.* 13, 261 (**2001**).
9. M. Chatterjee and A. Patra, *J. Am. Ceram. Soc.* 84, 1439 (**2001**).
10. H.-L. Li, Y.-C. Zhu, S.-G. Chen, O. Palchik, J.-P. Xiong, Y. Koltypin, Y. Gofer, and A. Gedanken, *J. Sol. State Chem.* 172, 102 (**2003**).
11. V. Ptatschek, C. Schmidt, M. Lerch, G. Muller, L. Spanhel, A. Emmerling, J. Fricke, A. H. Foitzik, and E. Langer, *Ber. Bunsenges. Phys. Chem.* 102, 85 (**1998**).
12. S. Gorer and G. Hodes, *J. Chem. Phys.* 98, 5338 (**1994**).
13. N. Gaponik, D. V. Talapin, A. L. Rogach, K. Hoppe, E. V. Shevchenko, A. Kornowski, A. Eychmuller, and H. Weller, *J. Phys. Chem. B* 106, 7177 (**2002**).
14. A. L. Rogach, N. A. Kotov, D. S. Koktysh, A. S. Susha, and F. Caruso, *Colloids and Surfaces A: Physicochemical and Engineering Aspects* 202, 135 (**2002**).
15. D. V. Talapin, A. L. Rogach, I. Mekis, S. Haubold, A. Kornowski, M. Haase, and H. Weller, *Colloids and Surfaces A: Physicochemical and Engineering Aspects* 202, 145 (**2002**).
16. Y.-W. Cao and U. Banin, *Angew. Chem. Int. Ed.* 38, 3692 (**1999**).
17. K. Koga, T. Ikeshoji, and K.-C. Sugawara, *Phys. Rev. Lett.* 92, 115507-1 (**2004**).
18. A. Burnin and J. J. BelBruno, *Chem. Phys. Lett.* 362, 341 (**2002**).
19. A. Nakajima, N. Zhang, H. Kawamata, T. Hayase, K. Nakao, and K. Kaya, *Chem. Phys. Lett.* 241, 295 (**1995**).
20. M. Alberti, O. Sedo, and J. Havel, *Polyhedron* 22, 2601 (**2003**).
21. Q. Sun, Q. Wang, T. M. Briere, V. Kumar, and Y. Kawazoe, *Phys. Rev. B* 65, 235417-1 (**2002**).
22. G. Seifert, P. W. Fowler, D. Mitchell, D. Porezag, and Th. Frauenheim, *Chem. Phys. Lett.* 268, 352 (**1997**).
23. V. V. Pokropivny, V. V. Skorokhod, G. S. Oleinik, A. V. Kurdyumov, T. S. Bartnitskaya, A. V. Pokropivny, A. G. Sisonyuk, and D. M. Sheichenko, *J. Solid State Chem.* 154, 214 (**2000**).
24. O. Stephan, Y. Bando, A. Loiseau, F. Willamie, N. Shramchenko, T. Tamiya, and T. Sato, *Appl. Phys. A* 67, 107 (**1998**).
25. T. Oku, A. Nishiwaki, I. Narita, and M. Gonda, *Chem. Phys. Lett.* 380, 620 (**2003**).
26. Q. Sun, Q. Wang, P. Jena, B. K. Rao, and Y. Kawazoe, *Phys. Rev. Lett.* 90, 135503-1 (**2003**).
27. G. Belomoin, J. Therrien, A. Smith, S. Rao, R. Twesten, S. Chaieb, M. H. Nayfeh, L. Wagner, and L. Mitas, *Appl. Phys. Lett.* 80, 841 (**2002**).
28. A. Kasuya, R. Sivamohan, Yu. Barnakov, I. Dmitruk, T. Nirasawa, V. Romanyuk, V. Kumar, S. Mamykin, K. Tohji, B. Jeyadevan, K. Shinoda, T. Kudo, O. Terasaki, Zh. Liu, R. Belosludov, V. Sundararajan, and Y. Kawazoe, *Nat. Mater.* 3, 99 (**2004**).
29. Y.-M. Koo, Y.-K. Choi, K.-H. Lee, and K.-W. Jung, *Bull. Korean Chem. Soc.* 23, 309 (**2002**).
30. C. Landes and M. A. El-Sayed, *J. Phys. Chem. A* 106, 7621 (**2002**).
31. M. V. Artemyev, A. I. Bibik, L. I. Gurinovich, S. V. Gaponenko, and U. Woggon, *Phys. Rev. B* 60, 1504 (**1999**).
32. H. Wang, A. Tashiro, H. Nakamura, M. Uehara, M. Miyazki, T. Watrai, and H. Maeda, *J. Mater. Res.* 19, 3157 (**2004**).
33. J. H. Yoon, W. S. Chae, S. J. Im, and Y. R. Kim, *Mater. Lett.* 59, 1430 (**2005**).
34. A. W. Castleman, Jr., and K. H. Bowen, Jr., *J. Phys. Chem.* 100, 12911 (**1996**).
35. H. W. Kroto, J. R. Heath, S. C. O'Brien, R. F. Curl, and R. E. Smalley, *Nature* 318, 162 (**1985**).
36. W. Kraetschmer, L. D. Lamb, K. Fostiropoulos, and D. R. Huffman, *Nature* 347, 27 (**1990**).
37. J. O. Joswig, M. Springborg, and G. Seifert, *J. Phys. Chem. B* 104, 2617 (**2000**).
38. K. Leung and K. B. Whaley, *J. Chem. Phys.* 110, 11012 (**1999**).
39. K. Eichkorn and R. Ahlrichs, *Chem. Phys. Lett.* 288, 235 (**1998**).
40. U. Rothlisberger, W. Andreoni, and M. Parrinello, *Phys. Rev. Lett.* 72, 665 (**1994**).

Received: 3 March 2008. Accepted: 24 March 2008.

RESEARCH ARTICLE

Takashi Kandori
Graduate School of Engineering,
Tohoku University,
6-6 Aramaki-Aoba,
Aoba-ku, Sendai 980-8579, Japan

Toshiyuki Hayase[1]
Institute of Fluid Science,
Tohoku University,
2-1-1 Katahira,
Aoba-ku, Sendai 980-8577, Japan

Kousuke Inoue

Kenichi Funamoto

Takanori Takeno

Institute for International Advanced
Interdisciplinary Research,
International Advanced Research and
Education Organization,
Tohoku University,
6-3 Aramaki-Aoba,
Aoba-ku, Sendai 980-8578, Japan

Makoto Ohta
Institute of Fluid Science,
Tohoku University,
2-1-1 Katahira,
Aoba-ku, Sendai 980-8577, Japan

Motohiro Takeda
Graduate School of Medicine,
Tohoku University,
2-1 Seiryo-machi,
Aoba-ku, Sendai 980-8574, Japan

Atsushi Shirai
Institute of Fluid Science,
Tohoku University,
2-1-1 Katahira,
Aoba-ku, Sendai 980-8577, Japan

Frictional Characteristics of Erythrocytes on Coated Glass Plates Subject to Inclined Centrifugal Forces

In recent years a diamond-like carbon (DLC) film and a 2-methacryloyloxyethyl phosphorylcholine (MPC) polymer have attracted attention as coating materials for implantable artificial organs or devices. When these materials are coated on vascular devices, compatibility to blood is an important problem. The present paper focuses on friction characteristics of erythrocytes to these coating materials in a medium. With an inclined centrifuge microscope developed by the authors, observation was made for erythrocytes moving on flat glass plates with and without coating in a medium of plasma or saline under the effect of inclined centrifugal force. Friction characteristics of erythrocytes with respect to these coating materials were then measured and compared to each other to characterize DLC and MPC as coating materials. The friction characteristics of erythrocytes in plasma using the DLC-coated and noncoated glass plates are similar, changing approximately proportional to the 0.5th power of the cell velocity. The cells stick to these plates in saline as well, implying the influence of plasma protein. The results using the MPC-coated plate in plasma are similar to those of the other plates for large cell velocities, but deviate from the other results with decreased cell velocity. The results change nearly proportional to the 0.75th power of the cell velocity in the range of small velocities. The results for the MPC-coated plate in saline are similar to that in plasma but somewhat smaller, implying that the friction characteristics for the MPC-coated plate are essentially independent of plasma protein. [DOI: 10.1115/1.2948420]

Keywords: erythrocytes, friction characteristics, inclined centrifuge microscope, DLC, MPC polymer, glass plate, plasma

1 Introduction

Blood flow in microcirculation plays an important role in supplying tissues with nutrients and removing metastases. Extensive physiological research has been carried out to examine blood flow in microcirculation focusing on the complex interaction between blood cells, plasma proteins, and glycocalyx in the endothelial surface layer [1,2]. Numerical analysis has been performed for cell motion in a blood capillary considering the interaction between the cell and the endothelial surface layer [3], but there have been little experimental measurement data of friction characteristics to date. It is critically important to develop a method to measure this friction force acting on the blood cells moving along the vessel surface.

The centrifuge microscope enables us to observe cells under centrifugal force [4], and, to date, several different types of centrifuge microscope have been developed [5]. These devices have been used to investigate various cell characteristics, for example, the mechanical properties of the Echinoderm egg [6], the motive force of paramecia [7], and the force-velocity relation of muscle fibers [8]. However, all existing centrifuge microscopes are designed such that the direction of cell deformation or movement and the direction of centrifugal force are identical, and the magnitude of the centrifugal force is the only parameter to be specified (see Fig. 1(*a*)). The present study uses the inclined centrifuge microscope [9], which enables us to observe cells on an inclined plane while specifying the tangential and normal force components of the centrifugal force independently (Fig. 1(*b*)). In order to gain a fundamental understanding of the blood cell interaction

[1]Corresponding author.
Contributed by the Bioengineering Division of ASME for publication in the JOURNAL OF BIOMECHANICAL ENGINEERING. Manuscript received August 23, 2007; final manuscript received March 11, 2008; published online July 14, 2008. Review conducted by Fumihiko Kajiya.

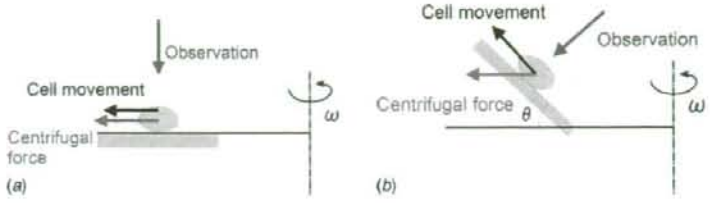

Fig. 1 Comparison between conventional and inclined centrifuge microscope: (*a*) conventional centrifuge microscope and (*b*) inclined centrifuge microscope

mentioned above, the present study investigated the friction characteristics of erythrocytes moving along material-coated glass plates in plasma or saline using the inclined centrifuge microscope.

In recent years materials for coating implantable artificial organs or devices have attracted attention. Among them this paper deals with diamond-like carbon (DLC) film [10] and 2-methacryloyloxyethyl phosphorylcholine (MPC) polymer [11]. DLC is one of the carbon based coatings with amorphous structure, which has properties similar to diamond. It has good resistance to corrosion and wear, low coefficient of friction, low partner aggressiveness, superflat smoothness, a thin film, and insulation properties. MPC was developed to create biomembrane structures artificially. It has a phosphorylcholine base that has a phospholipid polar group side chain and has a characteristic to restrain proteinaceous absorption.

When the DLC or MPC polymer is coated on vascular devices, compatibility to blood is an important problem. The present paper focuses on friction characteristics of erythrocytes to these coating materials in a medium. The inclined centrifuge microscope is used first to observe the motion of erythrocytes moving on flat glass plates with and without coating of DLC or MPC polymer in a medium of plasma or saline under the effect of centrifugal force at an angle with respect to the plate. Friction characteristics of erythrocytes to these materials are then measured and compared with each other to characterize DLC and MPC polymer as a coating material from the viewpoint of the friction property of erythrocytes.

2 Experimental Apparatus and Principle

2.1 Inclined Centrifuge Microscope. A schematic and specifications of the inclined centrifuge microscope system are shown in Fig. 2 and Table 1, respectively. In order to improve measurement performance, several components of the original equipment [9] have been replaced in the present system. A pair of inclined containers of inner dimension of $10 \times 8 \times 1$ mm^3 (width × length × height) is mounted on the rotor of the centrifuge (KUBOTA, Model 1120). One of the two containers is filled with a medium containing blood cells and the other container remains empty. The rotation speed of the rotor is measured using a digital tachometer (ONO SOKKI, TM-2110, error: 0.02%). A reference signal of rotation, which is generated by a laser diode (NEO ARK, LDP-6930C) and a detector (NEO ARK, RD-102), and is delayed through a pulse generator (Hewlett-Packard, HP81101A, 50 MHz) and a signal synthesizer (NF Circuit Design Block, WF1944), triggers an yttrium aluminum garnet (YAG) laser (KANOMAX, SPIV-30-20-ATT, 3 ns/pulse, 30 mJ/pulse) and a charge coupled device (CCD) camera (Ikegami, SKC-141, 15 fps, 145 megapixels). The exposure time of the CCD camera is fixed at 1/8000 s and the exposure timing is controlled to accurately synchronize with the rotation. The laser beam, which is guided through an optical fiber (NIKON, GFLG-5), illuminates the container for a very short interval of 3 ns during the exposure time of the CCD camera at the same angular position of the spinning rotor so that a still image of the plate can be observed. Erythrocytes moving on the plate are observed through a microscope (NIKON, CM-10) with objectives (Olympus, Cplan Fl 10× and CF Plan EPI SLWD 50×), the light axis of which is adjusted normal to the plate at an angle of θ from the horizontal plane. The microscope was remodeled to change the optical axis 90 deg by mirroring at the connecting point of the objective lens. The images are sent to a PC and stored on its hard drive.

In each measurement, 100 sequential images with an interval of the smallest multiple of the rotation period larger than 1/15 s were obtained. Each image was digitized into 1392 × 1024 pixels with a 256-level monochrome gradation and a diameter of 0.65 μm/pixel for the 10× objective lens. Fluctuation of the images due to inevitable error in synchronization was removed by translating the images based on grid lines of 5 μm in width etched on the back of the plates. The image data were

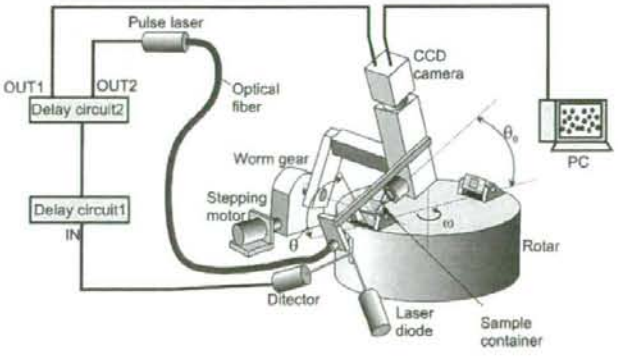

Fig. 2 Schematic of the inclined centrifuge microscope system

Table 1 Specifications of inclined centrifuge microscope

Angle of microscope	θ_0	0–50 deg
Angle of base plate	θ	40–90 deg
Angular frequency	ω	0–1257 rad/s
Magnification on 17 in monitor (10× and 50× objective lens)		×255, ×1275
Rotation radius	r_0	5.43×10^{-2} m
Rotation speed	N	0–12,000 rpm

processed by the PTV software program (Nexus, PIV EXPERT 2000) to obtain the velocity vectors of the erythrocytes. After the removal of background noise and smoothing, centers of gravity of all erythrocytes were obtained. The particle tracing velocimetry method was then applied in order to determine the velocity vectors of all the cells based on the distribution of cell centers at two time instants. The cell velocity is evaluated by the velocity component parallel to the tangential force since the rotational velocity component is strongly affected by the fluctuation in synchronization.

2.2 Principle of Friction Force Measurement. A schematic of the sample container is shown in Fig. 3. The plate is placed at the bottom of the container, which is inclined at an angle of θ from the horizontal plane (Fig. 3(*a*)). The container is filled with a medium (plasma or saline) in which erythrocytes have been dispersed. By applying rotation at an angular velocity ω, the cells move in a radial direction under the effect of centrifugal force F described as

$$F=(\rho_r-\rho_m)V_r r_0\omega^2 \tag{1}$$

where ρ_r, ρ_m are the densities of the erythrocyte and the medium, respectively, V_r is the volume of the cell (Table 2), and r_0 is the rotation radius (Table 1). Note that we consider the case in which the effect of gravitation is negligible and the rotation radius is assumed to be constant. After the cells contact the plate, the centrifugal force on each cell is naturally divided into two components; the normal force F_N and the tangential force F_T (Fig. 3(*b*)) as

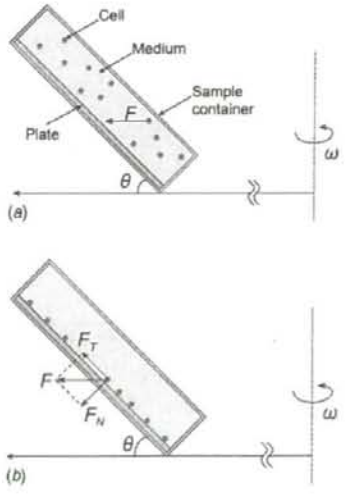

Fig. 3 Principle of friction force measurement in a rotating field: (*a*) initial state and (*b*) steady-state movement of erythrocytes

Table 2 Physical properties of specimen

Erythrocytes	
Diameter d_r	8.4×10^{-6} m
Height h_r	2.4×10^{-6} m
Volume V_r	8.7×10^{-17} m^3
Density ρ_r	1087 kg/m^3
Plasma	
Density ρ_p	1025 kg/m^3
Viscosity μ_p	1.2×10^{-3} Pa s
Saline	
Density ρ_s	998.2 kg/m^3
Viscosity μ_s	1.01×10^{-3} Pa s

$$F_N=F\sin\theta,\quad F_T=F\cos\theta \tag{2}$$

The normal force F_N balances the reaction from the plate, and the tangential force F_T accelerates the cell along the plate. When the cell velocity U reaches a steady value, the tangential force F_T is equal to the sum of the friction force F_T^* from the plate and the drag force f_D from the medium above the cell as

$$F_T=F_T^*+f_D \tag{3}$$

Precisely modeling the drag force for the shape of an actual erythrocyte is difficult. Since the Reynolds number based on the diameter and velocity of the cell and on the kinematic viscosity of the medium is less than 10^{-3} for the condition examined in the present study, we use the drag coefficient C_D of the Stokes equation for a sphere [12],

$$f_D=C_D(h_r,d_r)\frac{1}{2}\rho U^2,\quad C_D=24/R_e \tag{4}$$

where h_r and d_r denote the height and the diameter of the erythrocyte, respectively (Table 2).

As the force components F_N and F_T are specified arbitrarily by adjusting the angle of the container θ and the angular velocity ω. measuring the cell velocity U for a variety of force conditions gives the friction characteristics of the erythrocytes moving along the plate. A finite time is required before the cells attain a steady velocity with all forces in equilibrium.

By the assumption that the friction force is approximately described as the viscous friction of the uniform shear flow between the cell and the plate, we have the following equation:

$$F_T^*=\mu\cdot\dot{\gamma}\cdot\pi d_r^2/4 \tag{5}$$

where $\dot{\gamma}$ is the equivalent shear rate of the flow in a gap between the cell and the plate. The equivalent gap width h_g is given as

$$h_g=U/\dot{\gamma} \tag{6}$$

3 Materials and Methods

Human venous blood was sampled to a vacuum blood-collecting vessel (NIPRO NEO TUBE PET) from an informed healthy male volunteer of 24 years old. The blood anticoagulated by citric acid sodium (3.13%) was centrifuged (1000 g, 10 min) to separate plasma and erythrocytes. The plasma was centrifuged again in the same manner to purify it. A separate plasma and saline were then prepared as two mediums. Separated erythrocytes were distributed in the mediums at a volumetric concentration of 0.01%. The *p*H of the sample was 7.5 ± 0.1. The experiment was performed within 6 h after blood sampling and at a constant room temperature of 20 ± 1 °C. The physical properties of the materials are summarized in Table 2. The density of erythrocytes and that of the plasma are referred from our former study [9], whereas the other properties were obtained from literature [13].

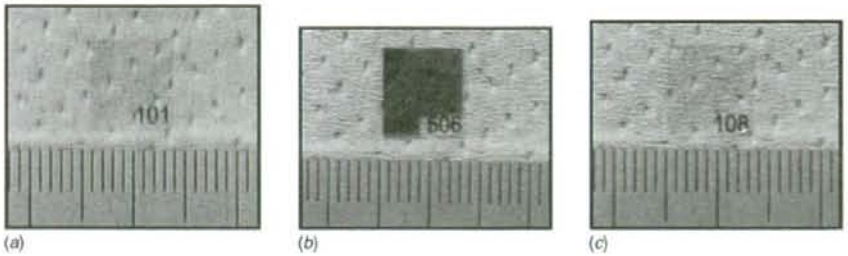

(a) (b) (c)

Fig. 4 Sample plates (small division=1 mm): (*a*) MPC-coated plate, (*b*) DLC-coated plate, and (*c*) non-coated plate

Pieces of cover glass made of synthetic quartz (Takahashi Giken Glass, 0.15 mm thickness) were used as the plates. Some of them were coated with DLC or MPC polymer. DLC coating was fabricated by chemical vapor deposition (CVD) technique. The deposition was performed for 20 min under the condition of 2.2 $\times 10^{-2}$ torr and −700 V of substrate self-bias voltage. A methane gas was used as a precursor gas. MPC polymer was coated on a different plate by putting the plate into PMB ethanol solution (0.2 wt %) and drying it naturally. The PMB ethanol is a mixture of non-water-soluble PMB30 and water-soluble PMB80 in a ratio of 9:1.

Figure 4 shows photographs of (*a*) a glass plate coated with MPC polymer (MPC-coated plate), (*b*) a glass plate coated with DLC (DLC-coated plate), and (*c*) a glass plate without coating (noncoated plate), respectively. The MPC-coated plates look the same as the noncoated plates. The DLC-coated plates are colored light brown but transparent.

Surface roughness of a noncoated plate and a DLC-coated plate was measured with an atomic force microscopy (AFM) (Veeco Enviroscope equipped with the NanoScope IV Controller). As shown in Fig. 5 the DLC-coated plate has larger roughness than the noncoated plate, but is still very smooth with roughness less than 10 nm. Since the probe used in the measurement was not applicable to soft surfaces, the surface roughness of MPC-coated plates was not measured.

4 Results

The motion of the erythrocytes on the three kinds of plates was first observed by using the 50× objective lens of the inclined centrifuge microscope. The friction characteristics were then measured by the 10× objective lens. In the experiment, tangential force component F_T was set between 2.5 pN and 40 pN while maintaining the normal force component F_N at 47 pN.

Figure 6 shows a snapshot of a motion picture in which erythrocytes (large circles) are moving upward in the figure on the MPC-coated plate in the medium of plasma under the effect of centrifugal force with a tangential force component F_T of 35 pN and a normal force component F_N of 47 pN. As mentioned above the tangential force component drives the cells to move on the plate and the normal force component pushes the cells on the plate. In the figure, the configurations of erythrocytes are clearly defined including a dark part in the center corresponding to a typical concave shape. The small dots in the figure are most likely aggregations of fibrinogen in plasma. Similar results were obtained for the noncoated plate and the DLC-coated plate under the same conditions.

For a relatively small tangential force of F_T=5 pN, some differences appear in the motion of erythrocytes between the plates. All the cells move on the MPC-coated plate, but some cells rest on the noncoated plate and more cells rest on the DLC-coated plate. The velocity of cells on the MPC-coated plate was larger than that of the others. The motion of moving cells on the DLC-coated plate fluctuated in a transverse direction in comparison with the other cases.

We then replaced plasma with saline as the medium. Figures 7(*a*) and 7(*b*) show the results for the MPC-coated and the DLC-coated plates, respectively, where F_T=30 pN and F_N=47 pN. Cells on the MPC-coated plate move smoothly but those on the DLC-coated plate stick to the plate stretching in the tangential force direction due to centrifugal force. The results of the noncoated plate were similar to that of the DLC-coated plate.

Next we measured the velocities of the cells to evaluate the friction characteristics of erythrocytes on the plates. In order to

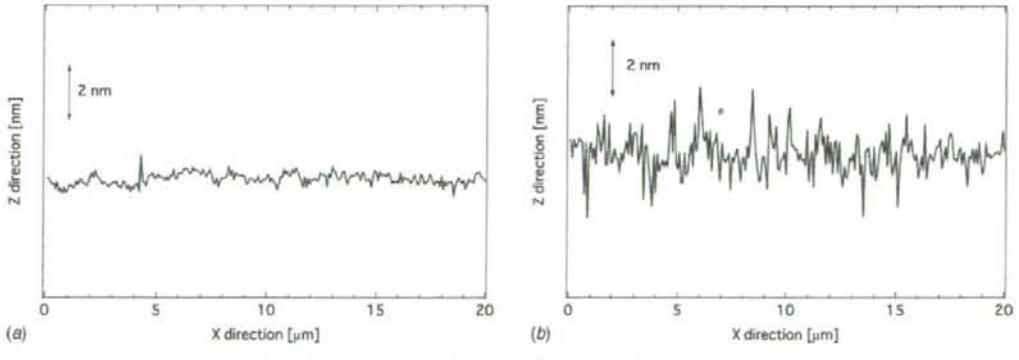

Fig. 5 Roughness of sample plates measured by AFM: (*a*) noncoated plate and (*b*) DLC-coated plate

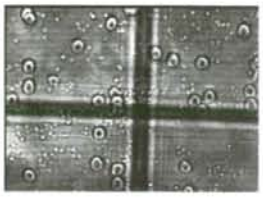

Fig. 6 Behavior of erythrocytes in plasma on MPC-coated plate (F_T=35 pN, F_N=47 pN)

observe a sufficient number of cells we used the 10× objective lens. The normal force was fixed at F_N=47 pN and the tangential force F_T was set at 5 pN intervals between 5 pN and 40 pN using plasma as a medium on the MPC-coated, DLC-coated, and noncoated plates, and at F_T=2.5, 5, 10, 20, 30 pN using saline as a medium on the MPC-coated plate.

Figure 8 is an example of 1 of 100 sequentially captured images for F_T=35 pN using plasma on the noncoated plate. These images were processed by the PTV software to obtain the velocities of cells using two sequential images. The typical number of velocities of cells obtained on the image was 140 in the present work. The mean value and the standard deviation of the velocities of cells obtained in each image are plotted in Figs. 9(*a*) and 9(*b*), respectively. By averaging these data we obtained the mean value and the standard deviation of the cell velocities for one experimental condition.

Figures 10(*a*)–10(*c*) show the mean velocity of cells with the tangential force for the MPC-coated, DLC-coated, and noncoated plates, respectively. The open symbol represents the results for plasma as the medium, while the closed symbol in Fig. 10(*a*) represents the results for saline. Each plot is based on the average value of four measurements of the same blood sample. For the plasma medium, the measurement was performed more than once using the blood of the same person sampled on different days. A pair of plots at the same F_T in a range of 10–40 pN represent the results three months apart. There are no data with saline as a medium for DLC-coated and noncoated plates since all the cells stick to the plates under this condition.

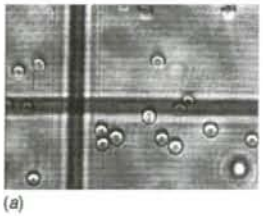

(*a*)

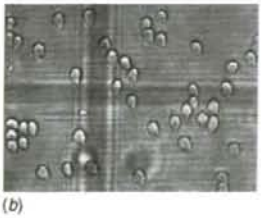

(*b*)

Fig. 7 Behavior of erythrocytes in saline (F_T=30 pN, F_N=47 pN): (*a*) MPC-coated plate and (*b*) DLC-coated plate

Fig. 8 Behavior of erythrocytes in plasma on noncoated plate (F_T=30 pN, F_N=47 pN).

By introducing the above results into Eq. (3), we obtained the friction force working between the cells and the plate. Equivalent shear rate and gap width were obtained from Eqs. (5) and (6). Figure 11(*a*) shows the friction force and the equivalent shear rate as a function of the mean cell velocity for the MPC-coated, DLC-coated, and noncoated plates in plasma and the MPC-coated plate in saline. Figure 11(*b*) shows the corresponding results for the equivalent gap width.

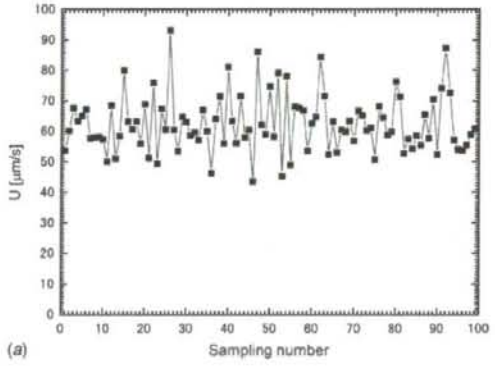

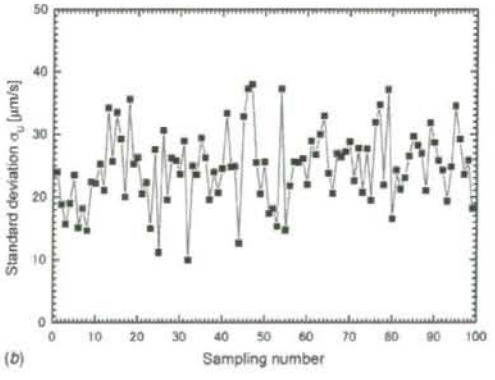

Fig. 9 Variation of mean value and standard deviation of velocity of erythrocytes in plasma on noncoated plate (F_T =30 pN, F_N=47 pN): (*a*) mean value and (*b*) standard deviation